Journal of Alloys and Compounds 504 (2010) 89–101

Contents lists available at ScienceDirect

Journal of Alloys and Compounds

journal homepage: www.elsevier.com/locate/jallcom

Decomposition behavior of unmilled and ball milled lithium alanate ($LiAlH_4$) including long-term storage and moisture effects

R.A. Varin*, L. Zbroniec

Department of Mechanical and Mechatronics Engineering, University of Waterloo, Waterloo, Ontario, Canada N2L 3G1

ARTICLE INFO

Article history:
Received 25 April 2010
Received in revised form 5 May 2010
Accepted 7 May 2010
Available online 20 May 2010

Keywords:
Solid state hydrogen storage
Hydrogen storage materials
Desorption temperature and kinetics
Lithium alanate ($LiAlH_4$)
Ball milling
X-ray diffraction (XRD)
Differential scanning calorimetry (DSC)

ABSTRACT

A comprehensive study of the decomposition behavior of as received and mechanically (ball) milled $LiAlH_4$ has been carried out using differential scanning calorimetry (DSC), X-ray diffraction (XRD) and volumetric hydrogen desorption in a Sieverts-type apparatus. Alfa Aesar $LiAlH_4$ powder investigated in this work has the average particle size of 9.9 ± 5.2 μm as compared to 50–150 μm for Sigma–Aldrich $LiAlH_4$ investigated by Ares et al. [9]. High energy ball milling reduced the particle size of the present $LiAlH_4$ to 2.8 ± 2.3 μm. In general, comparing the results of our microstructural studies with those reported by Ares et al. [9] it is clear that the morphology, microstructure and chemistry of $LiAlH_4$ can be very dissimilar depending on the supplier from which $LiAlH_4$ powder was purchased. We do not observe a partial decomposition of $LiAlH_4$ during milling up to 5 h under high energy impact mode. The observed melting of $LiAlH_4$ in a DSC test is a very volatile event where the liquid $LiAlH_4$ starts foaming and flowing out of the alumina crucible. After completion of solidification and desorption at temperatures above melting the powder resembles a lava rock. A thermal sectioning in DSC tests at pre-determined temperatures and subsequent XRD studies show that $LiAlH_4$ starts decomposing into Li_3AlH_6 immediately after melting. Li_3AlH_6 seems to be already solidified before it starts decomposing in the next stage. All volumetric desorption curves at the 120–300 °C range clearly exhibit a two-stage desorption process, Stage I and II. As received $LiAlH_4$ is able, in a fully solid state, to desorb at 120 °C under pressure of 0.1 MPa H_2 (atmospheric) as much as 7.1 wt.%H_2 within ~259,000 s (~72 h), i.e. ~93% of the purity-corrected H_2 content from the reactions in Stage I ($LiAlH_4(s) \rightarrow (1/3)Li_3AlH_6(s) + (2/3)Al(s) + H_2$) and Stage II ($(1/3)Li_3AlH_6(s) \rightarrow LiH + (1/3)Al + 0.5H_2$). The apparent activation energy for Stage I and II for unmilled $LiAlH_4$ is equal to ~111 and ~100 kJ/mol, respectively. For the ball milled $LiAlH_4$ the apparent activation energy for Stage I and II is slightly lower ~92.5 and ~92 kJ/mol, respectively. The water absorption up to 11.7% due to exposure to air for 1 h does not change in any drastic way the hydrogen desorption rate of ball milled $LiAlH_4$ in Stage I. Flammability tests show that the ball milled $LiAlH_4$ powder does not self-ignite on contact with air but can only be ignited by scraping the cylinder walls with a metal tool and then the powder burns with an open flame.

1. Introduction

One of the most critical issues to be solved before the full implementation of the hydrogen economy is hydrogen storage. It is imperative that it has to be solved before a technically and economically viable hydrogen economy can be established. Current methods of hydrogen storage such as compressed and liquid hydrogen have serious drawbacks as storage media [1]. In a long run, the most promising is hydrogen storage system based on solid hydrides or their mixtures (composites) having hydrogen capacities exceeding 6 wt.% and the enthalpies of decomposition/reaction within the 20–50 kJ/mol range [1]. A low enthalpy removes the thermodynamic barrier for hydrogen desorption although a kinetic barrier may still remain. The latter could be dealt with by using suitable catalysts. Hence, vigorous research efforts are necessary in that field.

Lithium alanate ($LiAlH_4$) hydride is one of the most interesting candidate hydrides for solid state hydrogen storage. $LiAlH_4$ has been classified by Graetz and Reilly [2], as belonging to the family of "kinetically stabilized hydrides" which are characterized by low reaction enthalpies and extremely high equilibrium hydrogen pressure at relatively low temperatures. They are metastable though and do not spontaneously decompose owing to not-well understood kinetic limitations. One of these kinetically stabilized hydrides is $LiAlH_4$ which has the following virtues: (a) a low density which allows for a high theoretical hydrogen capacity (~10.6 wt.%), (b) low decomposition enthalpies translating to low decomposition temperatures expected and (c) a relatively large theoretical hydro-

* Corresponding author. Tel.: +1 519 888 4567; fax: +1 519 885 5862.
E-mail address: ravarin@mecheng1.uwaterloo.ca (R.A. Varin).

0925-8388/$ – see front matter © 2010 Elsevier B.V. All rights reserved.
doi:10.1016/j.jallcom.2010.05.059

gen quantity of about 7.9 wt.% that could be liberated below 250 °C. Some drawbacks will include the presence of exothermic decomposition reaction, extremely high plateau pressure at relatively low temperatures which makes the hydride practically irreversible and relatively slow hydrogen desorption rates. The latter can be much improved by adding catalytic metal chlorides. This discovery led to massive research efforts on the effect of catalytic metal chlorides resulting in a large number of publications which are reviewed in [1]. However, it is important that the decomposition behavior of pristine $LiAlH_4$ must be clearly elucidated before one can try to improve its hydrogen storage properties by catalytic additives. This is an on-going research in our laboratory. The decomposition behavior of pristine $LiAlH_4$ and the effects of ball milling on its behavior have been investigated for some time [3–9]. However, some aspects of decomposition behavior of pristine $LiAlH_4$ still remain poorly understood, such as, for example, the problem of mechanically driven partial decomposition of $LiAlH_4$ during ball milling [9].

For the first time a thorough morphological and microstructural investigations of the as received and ball milled powders are presented in this work. In order to assess the effect of milling energy on the microstructure and decomposition behavior ball milling was carried out under controlled milling conditions with varying energy using a magneto-mill [1]. A thermal sectioning in DSC at pre-determined temperatures combined with a phase analysis using X-ray diffraction was used to monitor the evolution of phases during thermal decomposition of as received and ball milled $LiAlH_4$. A volumetric hydrogen desorption analysis under a technological condition of atmospheric pressure of 0.1 MPa H_2 has been applied to study the decomposition behavior of as received and ball milled $LiAlH_4$. A very wide decomposition temperature range from 120 to 300 °C was studied. The apparent activation energy of hydrogen desorption was estimated using the JMAK (Johnson–Mehl–Avrami–Kolmogorov) theory of phase transformations. By comparison with powders used in [9] it is shown that profound morphological/microstructural differences exist between $LiAlH_4$ powders purchased from various suppliers which can affect milling conditions and subsequent decomposition properties which may lead to discrepancies between the results reported in the literature. An assessment of the exposure to moisture on the desorption behavior of $LiAlH_4$ and its flammability/pyrophoricity are also reported.

2. Experimental

As received commercial $LiAlH_4$ (97% purity) from Alfa Aesar was used in this work. Controlled Mechanical Milling (CMM) was carried out in ultra-high purity hydrogen gas atmosphere (purity 99.999%: O_2 < 2 ppm; H_2O < 3 ppm; CO_2 < 1 ppm; N_2 < 6 ppm; CO < 1 ppm; THC < 1 ppm) under ~600 kPa pressure in the magneto-mill Uni-Ball-Mill 5 manufactured by A.O.C. Scientific Engineering Pty Ltd., Australia [1,10–12]. In this particular ball mill the milling modes with varying milling energy can be achieved by using one or two strong NdFeB magnets, changing their angular positions and changing the number of hard steel balls (25 mm in diameter each) in a milling vial. In order to vary milling energy we used 1 magnet and 4 balls with the ball-to-powder weight ratio (R) ~40 (R40) as well as IMP68 mode with the ball-to-powder weight ratio R40 or R132 and the rotational speed of milling vial ~200 rpm. Fig. 1 shows a schematic set-up for a strong impact mode IMP68 with two magnets positioned at 6 and 8 o'clock, at the distance of 10 and 2 mm, respectively, from the milling vial (working distance – WD) and 4 hard steel balls in the vial. During milling for 15 min the vial was not cooled but during milling for 2 and 5 h the milling vial was continuously cooled using a fan.

After loading with powder, an air-tight milling vial with an O-ring, equipped with a pressure valve mounted in the vial's lid, was always evacuated and purged several times with ultra-high purity argon (Ar) gas (99.999% purity) before final pressurization with H_2. All the powder handlings were performed in a purged glove box in ultra-high purity argon atmosphere.

The crystalline structure of powders was characterized by Bruker D8 diffractometer using a monochromated Cu $K\alpha_1$ radiation (λ = 0.15406 nm) produced at an accelerating voltage of 40 kV and a current of 30 mA. The scan range was from 2θ = 10° to 90° and the scan rate was 3° min^{-1}. Powder was loaded into an argon-filled environmental holder in a glove box not allowing any exposure to the environment.

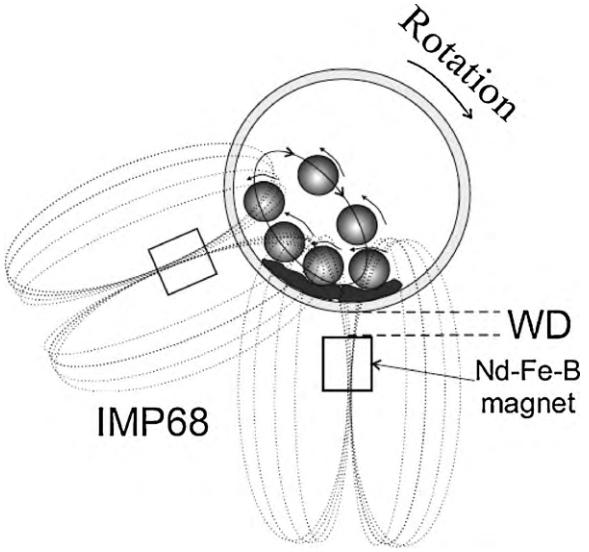

Fig. 1. A schematic of the cross-section of the milling vial and the approximate trajectories of the ball movement under IMP68 mode of milling in the magneto-mill Uni-Ball-Mill 5.

The nanograin/crystallite size of phases residing in the milled powders was calculated from the broadening of their respective XRD peaks. Since the Bragg peak broadening in an XRD pattern is due to a combination of grain refinement and lattice strains, it is customary to use computing techniques by means of which one can separate these two contributions. The separation of crystallite size and strain was obtained from Cauchy/Gaussian approximation by the linear regression plot according to the following equation [13]:

$$\frac{\delta^2(2\theta)}{\tan^2\theta} = \frac{K\lambda}{L}\left(\frac{\delta(2\theta)}{\tan\theta\sin\theta}\right) + 16e^2 \quad (1)$$

where the term $K\lambda/L$ is the slope, the parameter L is the mean dimension of the nanograin (crystallite) composing the powder particle, K is constant (~1) and e is the so-called "maximum" microstrain (calculated from the intercept), λ is the wave length and θ is the position of the analyzed peak maximum. The term $\delta(2\theta) = B[1-(b^2/B^2)]$ (rad) is the instrumental broadening-corrected "pure" XRD peak profile breadth [13] where B and b are the breadths in radians of the same Bragg peak from the XRD scans of the experimental and reference powder, respectively. They were calculated by the software Traces™ v. 6.5.1 as the full-widths at half maximum, FWHM, after background removal. A compound LaB_6, the National Institute of Standards and Technology (NIST) standard reference material (SRM) 660 was used as a reference for subtracting the instrumental broadening from FWHM. It must be noted that when the FWHM of the instrumental line profiles were obtained in this manner, the Bragg peaks for the LaB_6 SRM were at different 2θ angles than those of the analyzed phases in the milled powders. The interpolated FWHM values between angles for the SRM peaks were found using a calibration curve.

The images of powders were obtained using a high-resolution, field emission SEM (FE SEM) LEO 1530. The average size of the powder particles was calculated as the particle Equivalent Circle Diameter, ECD = $(4A/\pi)^{1/2}$, where A represents the projected particle area. The projected area was estimated by attaching loose powder to a sticky carbon tape and taking pictures under secondary emission (SE) mode in a LEO 1530. The SEM images were subsequently analyzed by the Image Tool software. Around 1200 particles were evaluated.

The hydrogen desorption was evaluated using a second generation volumetric Sieverts-type apparatus custom-built by A.O.C. Scientific Engineering Pty Ltd., Australia. This apparatus built entirely of austenitic stainless steel allows loading of a powder sample into a tightly sealed austenitic stainless steel sample reactor in a glove box under argon and subsequent transfer of the reactor to the main unit without any exposure to the environment. The weight of the powder sample in the desorption experiments was in the range of 20–30 mg. The calibrated accuracy of desorbed hydrogen capacity is about ±0.1 wt.%H_2 and that of temperature reading ±0.1 °C. Before starting the desorption test, the inner tubing of the apparatus and reactor were evacuated and purged 3 times with argon and finally with hydrogen. The moveable furnace of the apparatus was heated separately to the desired test temperature and subsequently inserted onto a sample reactor inside which an atmospheric pressure of 0.1 MPa H_2 was kept. Hence, the beginning of the desorption test was in reality pseudo-isothermal before the powder sample temperature reached the desired value. However, the calibrated time interval within which the powder sample in the reactor reaches the furnace temperature is ~400–600 s in the 100–450 °C range, which is quite negligible compared to the desorption completion time. Therefore, one can consider the test as being "isothermal" for any practical

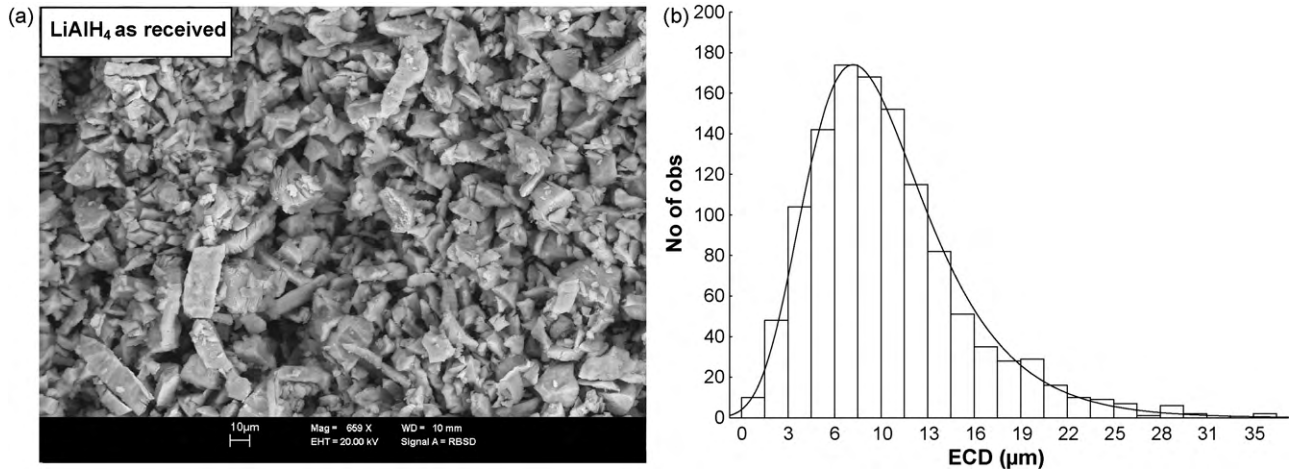

Fig. 2. (a) Scanning electron backscatter micrograph of the as received $LiAlH_4$ particles. (b) A fit of the as received $LiAlH_4$ particle distribution histogram by an extreme probability distribution function.

purposes at this range of temperatures. The amount of desorbed hydrogen was calculated from the ideal gas law as described in detail in [1]. Hydrogen desorption curves were also corrected for the hydrogen gas expansion due to the increase in temperature.

The activation energy for desorption process was estimated from the obtained Sieverts' desorption curves at corresponding temperatures using the Arrhenius plot of k values with temperature [1]:

$$k = k_0 e^{-E_A/RT} \tag{2}$$

where E_A is the activation energy, R is the gas constant and T is the temperature. The rate constant k was determined using the Johnson–Mehl–Avrami–Kolmogorov (JMAK) equation [1]:

$$\alpha = 1 - e^{-(k \cdot t)^{\eta}} \tag{3}$$

where η is the reaction exponent (the Avrami exponent) related to the transformation mechanism, taken as a free value characteristic for each individual temperature [1,14] rather than a fixed value for all temperatures, and α is the desorption fraction at time t.

The thermal behavior of powders was studied by differential scanning calorimetry (DSC) (Netzsch 404) of ~6 mg powder sample with heating rate of 10 °C/min and argon flow rate of 100 ml/min. The powder was transported to a DSC instrument in a glass vial filled with Ar then quickly loaded into an Al_2O_3 crucible with a lid and then into the air-tight DSC chamber. This operation took about 2–3 min and only for that short period of time the powder could be in contact with air.

The moisture effects were studied by exposing a powder of $LiAlH_4$ milled for 15 min under IMP68 mode to air with 47% relative humidity for 1 h. The mass of the powder was measured before and after exposure from which the percentage of absorbed H_2O was calculated.

Finally, it must be pointed out that all the tests described in the following sections were carried out within a couple of days from the completion of ball milling.

3. Results and discussion

3.1. Morphology and microstructure of $LiAlH_4$ before and after ball milling

Fig. 2a and b shows the SEM micrograph of the morphology and particle size distribution of the as received $LiAlH_4$ powder, respectively. The individual $LiAlH_4$ particles have a "blocky" shape which is most likely related to the monoclinic crystal lattice of $LiAlH_4$ (space group $P2_1c$) [7]. The size distribution seems to be quite uniform. The particle size distribution in Fig. 2b shows that the best fitting is obtained by the extreme value type I (maximum) distribution function [15]. The fitting by a log-normal function gave slightly worse fit. From measuring ~1200 particles in SEM the average ECD particle size with standard deviation (S.D.) is obtained as 9.9 ± 5.2 μm. It is to be pointed out that the morphology of the present as received $LiAlH_4$ purchased from Alfa Aesar is very different than that of $LiAlH_4$ powder investigated by Ares et al. [9] who purchased their powder from Sigma–Aldrich. The latter as received powder exhibited much larger particle sizes having a distinctly bi-modal distribution centered around ~50 and ~150 μm.

The effect of ball milling on the particle morphology of $LiAlH_4$ is shown in the SEM micrographs in Fig. 3a and b for a $LiAlH_4$ powder milled under high energy IMP68 mode for 2 h. Measuring of ~1200 particles at the magnification of 2 K gave the average ECD value of 2.8 ± 2.3 μm. Fig. 3b shows a particle size distribution histogram for

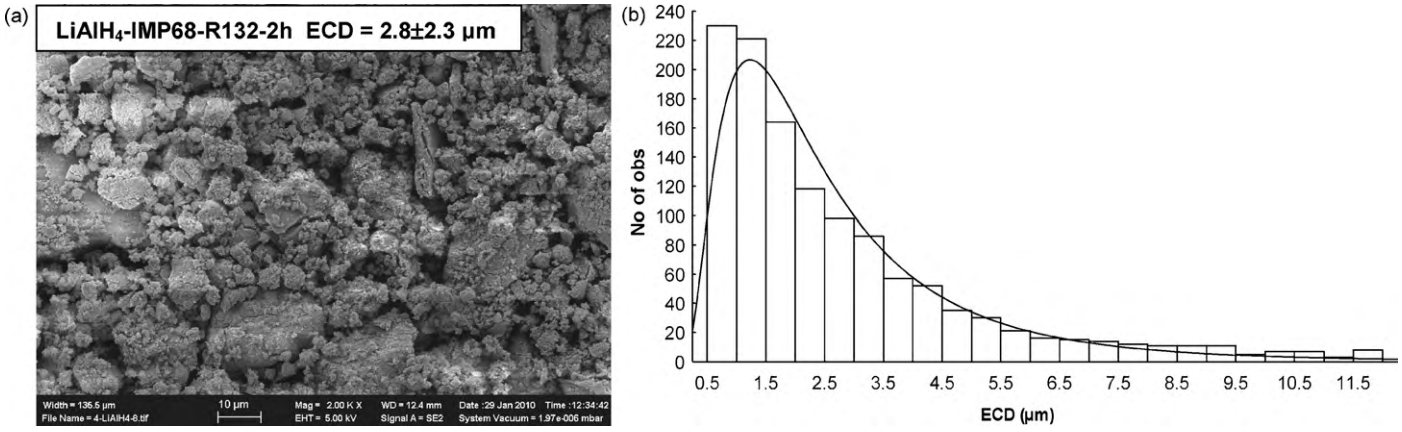

Fig. 3. (a) Scanning secondary electron micrograph of $LiAlH_4$ after ball milling for 2 h under high energy impact mode IMP68 with R132. (b) Particle size (ECD) distribution for milled powder.

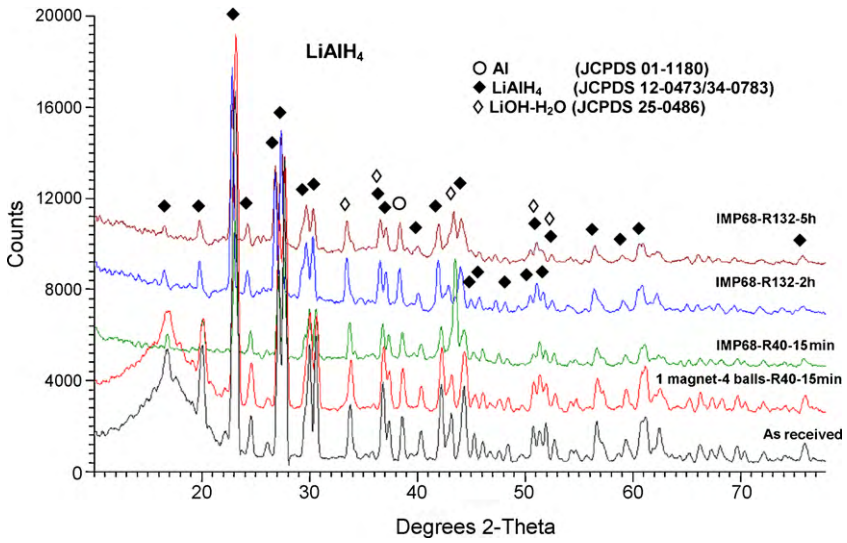

Fig. 4. XRD patterns of $LiAlH_4$ as received and ball milled under varying energy milling modes and milling times. JCPDS file numbers for phase identification are given in parenthesis.

this powder. As can be seen, in this case the best fit line is obtained by a classical log-normal function [15] rather than by the extreme value type I (maximum) as the one for the as received powder. A long ball milling of $LiAlH_4$ usually leads to more agglomeration and is not recommended. For example, the average ECD particle size for the powder milled for 20 h under high energy shearing mode (HES57) was observed to be $5.2 \pm 4.3\ \mu m$ [1].

It must be noted that the average ECD particle size of ball milled $LiAlH_4$ obtained in this work is much smaller than the average particle size reported by Ares et al. [9] which after 30 min of milling of their Sigma–Aldrich $LiAlH_4$ was $80 \pm 40\ \mu m$ and after 1.5 h of milling it was still $30 \pm 15\ \mu m$. Comparing with the milling results reported in [9] it is clear that the smaller initial as received particle size of $LiAlH_4$ powder in this work results in a greater particle size reduction during milling. Obviously, also the milling technique may be to a certain extent responsible for the final particle size reduction during milling. For comparison, Ares et al. [9] used Fritsch P7 planetary ball mill.

Fig. 4 shows the XRD patterns of $LiAlH_4$ after ball milling with varying milling energy (number of magnets and ball-to-powder weight ratio R) compared to the XRD pattern of as received $LiAlH_4$. The microstructure of as received $LiAlH_4$ comprises, besides $LiAlH_4$ also a small amount of Al and $LiOH–H_2O$. The former is most likely an impurity and $LiOH–H_2O$ might be a result of inadvertent contact of powder with air during handling despite the fact that all handling was done in a purged glove box filled with ultra-high purity Ar and powders for XRD tests were loaded into an environmental holder under ultra-high purity Ar. Similar observation was reported by Blanchard et al. [16] for $LiAlD_4$ (deuteride) where they also found $LiOH–H_2O$. In contrast, as received $LiAlH_4$ from Sigma–Aldrich studied by Ares et al. [9] did not contain any Al impurities but instead contained a small amount of LiCl impurity. Again, this comparison shows that $LiAlH_4$ obtained from different suppliers can have not only different morphology/microstructure but also different type of impurities which can be responsible for some differences in the results reported in the literature as discussed below.

It can be seen in Fig. 4 that the milling mode or R parameter does not affect the phase presence in any major way. Also, milling up to 5 h does not lead to a partial decomposition of $LiAlH_4$. Our finding is in accord with the results of Balema et al. [6] who reported that $LiAlH_4$ revealed good stability up to 35 h of high energy milling. They also observed a partial decomposition of $LiAlH_4$ into Li_3AlH_6, Al and H_2 during prolonged milling up to 110 h. It must, however, be pointed out that Andreasen et al. [8] claimed that a partial decomposition of $LiAlH_4$ might have occurred during milling up to 10 h although no clear evidence was presented to this claim. Ares et al. [9] reported that $LiAlH_4$ partially decomposed after ball milling for barely 1.5 h which was reflected in a diminution of hydrogen capacity as compared to as received $LiAlH_4$ although XRD patterns showed $LiAlH_4$ as the only phase existing in the milled powder. They also detected Al at the surface of particles. We do not confirm a partial decomposition of $LiAlH_4$ after milling up to 5 h as mentioned above. As shown in Fig. 4 in our Alfa Aesar powder Al seems to be an impurity and is not a product of decomposition since we do not observe a clear diminution of the overall hydrogen capacity for $LiAlH_4$ ball milled 15 min as compared to the as received powder as will be discussed later.

Table 1 shows the comparison of grain/crystallite size of $LiAlH_4$ before and after ball milling calculated from the broadening of diffraction peaks (Eq. (1)). Excellent coefficients of fit to Eq. (1) give a testimony to the accuracy of the method. The most interesting finding is that the grain/crystallite size of as received $LiAlH_4$ has an average size of ~30 nm and after milling under high energy mode IMP68 the grain sizes are, on average, larger than that of as received $LiAlH_4$. For powder milled using a continuous cooling of the vial the grain sizes are slightly smaller than those formed for non-cooled samples. Furthermore, low energy milling mode with 1 magnet does not change the grain size as compared to as received material. Such a behavior suggests some possibility of localized heating during high energy ball milling resulting in a grain growth of $LiAlH_4$. However, the amount of heat produced is still insufficient to induce a partial decomposition of $LiAlH_4$ during milling at least to the extent we could observe from the capacity changes. The grain size of present $LiAlH_4$ is different than that reported by Ares et al.

Table 1
Grain size of unmilled and ball milled $LiAlH_4$.

Milling mode	Cooling during milling	Grain size (nm)	R^2
As received	–	28	0.968
1 magnet–4 balls-R40–15 min	No	23	0.992
IMP68–R40–15 min	No	64	0.981
IMP68–R132–15 min	No	78	0.935
IMP68–R132–2 h	Yes	43	0.972
IMP68–R132–5 h	Yes	52	0.988

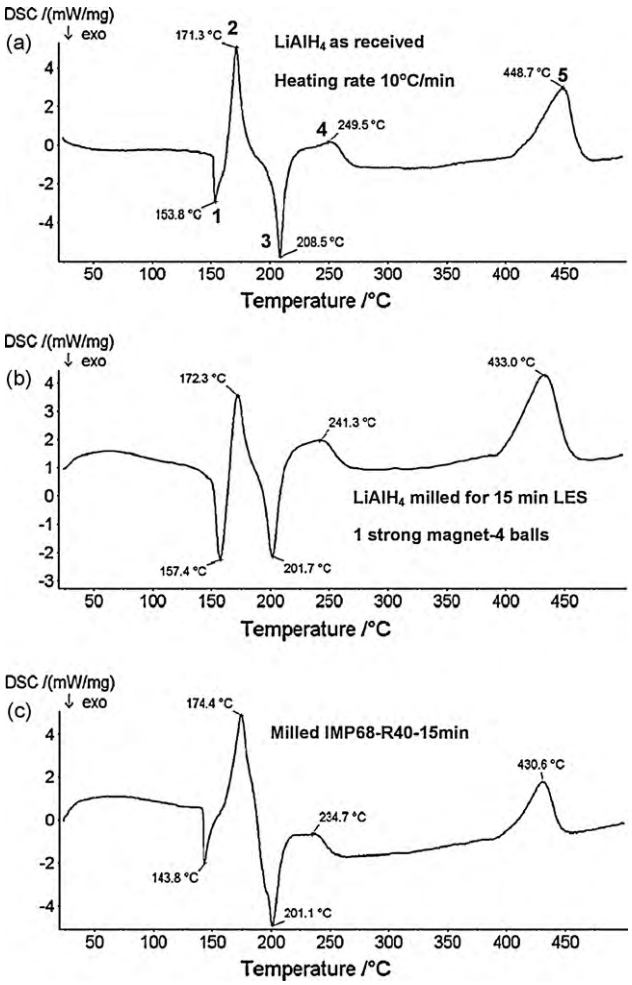

Fig. 5. DSC curves for $LiAlH_4$ as received and ball milled under varying energy milling modes. (a) As received, (b) milled for 15 min under low energy shearing (LES) mode with 1 magnet, 4 balls and R40 and (c) milled for 15 min under high energy milling mode IMP68 and R40. Heating rate is 10 °C/min.

[9] for their Sigma–Aldrich $LiAlH_4$ whose average as received grain (crystallite) size was greater than 300 nm and decreased to about 90 ± 30 nm after 30 min of milling with further milling having no influence on grain (crystallite) size.

It is clear from the comparison of microstructural investigations of the present $LiAlH_4$ with those reported by Ares et al. [9] that the morphology, microstructure and chemistry of $LiAlH_4$ can be very dissimilar depending on the supplier from which $LiAlH_4$ powder was purchased and may affect the storage properties.

3.2. Thermal decomposition and microstructural evolution during DSC test

Fig. 5 shows a comparison of DSC traces for as received $LiAlH_4$ and that milled under varying energy of milling. In agreement with the early studies of Block and Gray [3] and McCarty et al. [4] on the thermal decomposition of $LiAlH_4$, two distinct exotherms (designated 1 and 3 in Fig. 5a) and three endotherms (designated 2, 4 and 5 in Fig. 5a) are observed. All DSC curves regardless of milling mode exhibit these five thermal peaks. The first exotherm 1 was assigned by Block and Gray [3] to the reaction of the surface aluminum-hydroxyl groups owing to the presence of impurities of the following type

$$> \text{Al-OH} + \text{H–Al} < \rightarrow > \text{Al–O–Al} < + H_2 \quad (4)$$

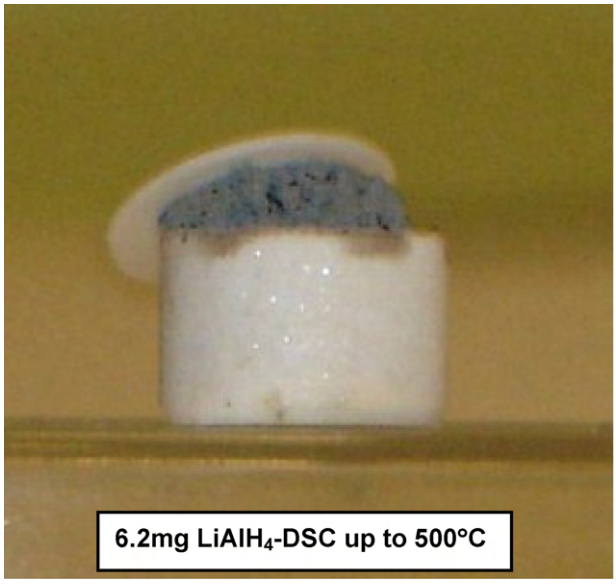

Fig. 6. Optical photo showing 6.2 mg of as received $LiAlH_4$ powder solidified after melting in an alumina crucible used for a DSC test. Heating rate is 10 °C/min.

The above reaction according to Block and Gray [3] was related to the evolution of a small quantity of hydrogen.

The endotherm (2) is commonly related to the melting of $LiAlH_4$ [1] according to

$$LiAlH_4(\text{solid}) \rightarrow LiAlH_4(\text{liquid}) \quad (5)$$

The melting of $LiAlH_4$ is a very volatile event. Fig. 6 shows an optical photograph of a small amount of as received $LiAlH_4$ powder which was tested in DSC at 10 °C/min up to 500 °C. Immediately after the beginning of melting the liquid $LiAlH_4$ started foaming and flowing out of the alumina crucible raising the alumina lid as can be seen in Fig. 6. The solidified powder obtained after desorption resembled a lava rock. The melting enthalpy of reaction (2) is quoted in the literature as 13 kJ/(mol $LiAlH_4$) [9] and 16.6 kJ/(mol $LiAlH_4$) [17].

In a molten state $LiAlH_4$ starts desorbing hydrogen in the following exothermic reaction [1]

$$LiAlH_4(l) \rightarrow (1/3)Li_3AlH_6(s) + (2/3)Al(s) + H_2 \quad (6)$$

where l-liquid and s-solid. According to a general consensus [1] reaction (6) proceeds with a theoretical hydrogen release of 5.3 wt.%. The enthalpy of reaction (6) is quoted as being equal to experimentally observed value of −14 kJ/(mol H_2) [9] and −10 kJ/(mol H_2) [18] or alternatively equal to the two calculated values of 9.79 and 3.46 kJ/mol [19]. The latter two values apparently correspond to an endothermic reaction rather than to an exotherm. It seems that there is some confusion regarding the nature of reaction (6).

Endothermic reaction (7) is supposed to occur completely in a solid state according to the following path [1]

$$(1/3)Li_3AlH_6 \rightarrow LiH + (1/3)Al + 0.5H_2 \quad (7)$$

It proceeds with a theoretical hydrogen release of 2.6 wt.%. Its enthalpy is quoted as being equal to 15 kJ/(mol H_2) [9] or 25 kJ/(mol H_2) [17]. It must be mentioned that at low heating rates in DSC of 1–2 °C/min some researchers reported no sign of melting [4,9] and the process of melting and solidification is substituted by one endothermic reaction [9].

Reactions (8a) and (8b) occur at temperatures around 400–450 °C [1] according to the following path

$$LiH \rightarrow Li + 0.5H_2 \quad (8a)$$

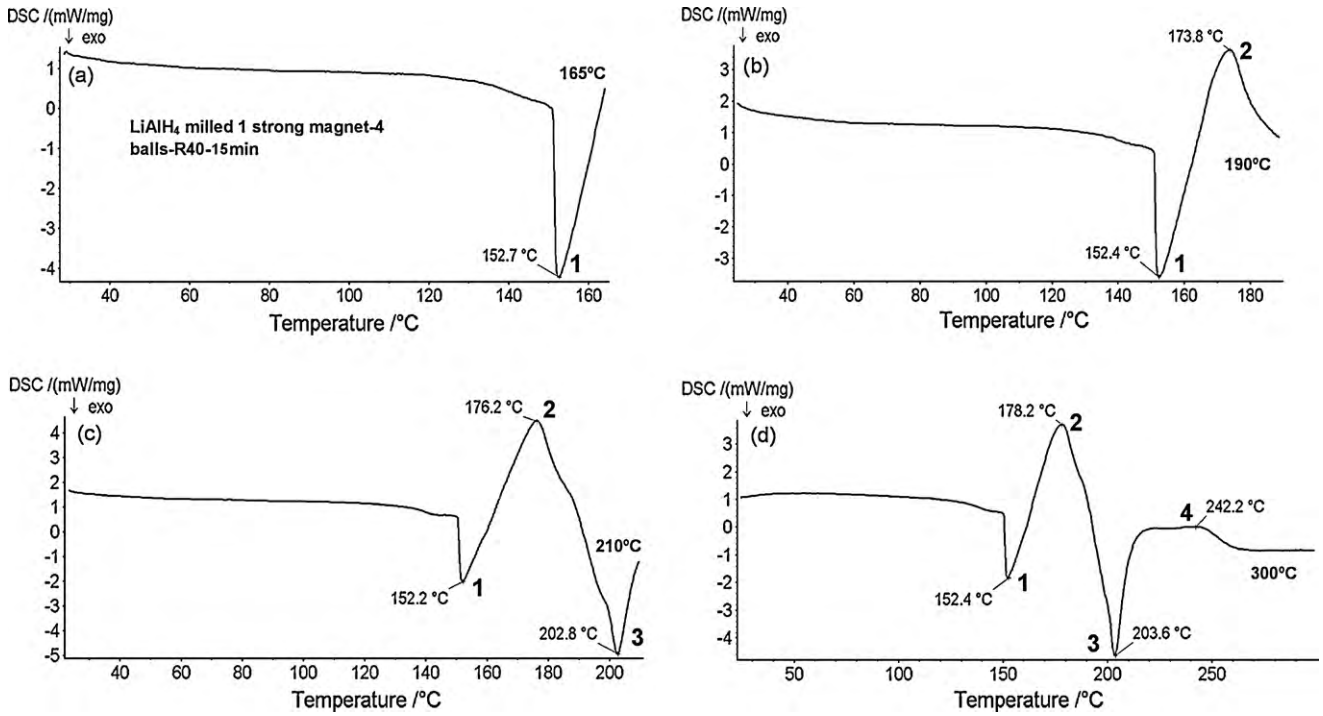

Fig. 7. Isothermal sectioning of DSC test for $LiAlH_4$ powder ball milled for 15 min under low energy shearing (LES) mode with one magnet, 4 balls and R40. (a) DSC test stopped at 165 °C (after peak 1), (b) DSC test stopped at 190 °C (after peak 2), (c) DSC test stopped at 210 °C (after peak 3), and (d) DSC test stopped at 300 °C (after peak 4). Heating rate is 10 °C/min.

or alternatively [19]

$$LiH + Al \rightarrow LiAl + 0.5H_2 \quad (8b)$$

with the enthalpy of 140 kJ/mol [18] for a LiH decomposition and a hydrogen release of 2.6 wt.%.

In order to shed more light on the nature of the above reactions we did a thermal sectioning in DSC at pre-determined temperatures. As shown in Fig. 7 each DSC test was stopped at a temperature of 165, 190, 210 and 300 °C beyond each reaction peak 1, 2, 3 and 4, respectively. After stopping the test the powder sample from a crucible was immediately taken for an XRD test. The corresponding XRD patterns are shown in Fig. 8. The sample heated up to 165 °C, beyond the peak (1) of reaction (4) (Fig. 7a), still shows the presence of a majority phase $LiAlH_4$ and minority impurity phases of Al and $LiOH–H_2O$ (same as in the as received powder in Fig. 4). On the basis of this pattern it is hard to verify whether or not reaction (4) indeed occurred. The sample heated up to 190 °C, just beyond the peak (2)

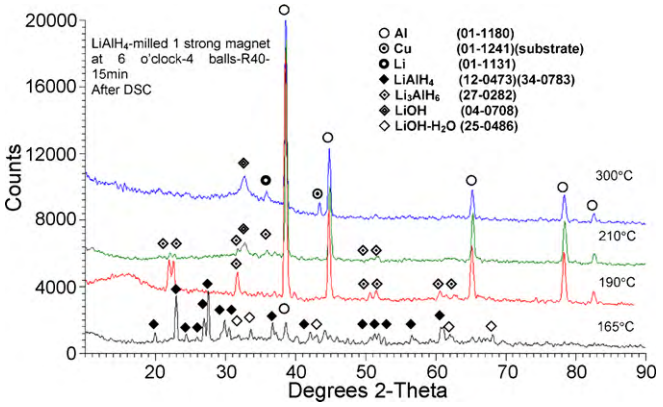

Fig. 8. XRD patterns taken from the powder sample obtained in a DSC thermal sectioning test up to 165, 190, 210 and 300 °C. JCPDS file numbers for phase identification are given in parenthesis.

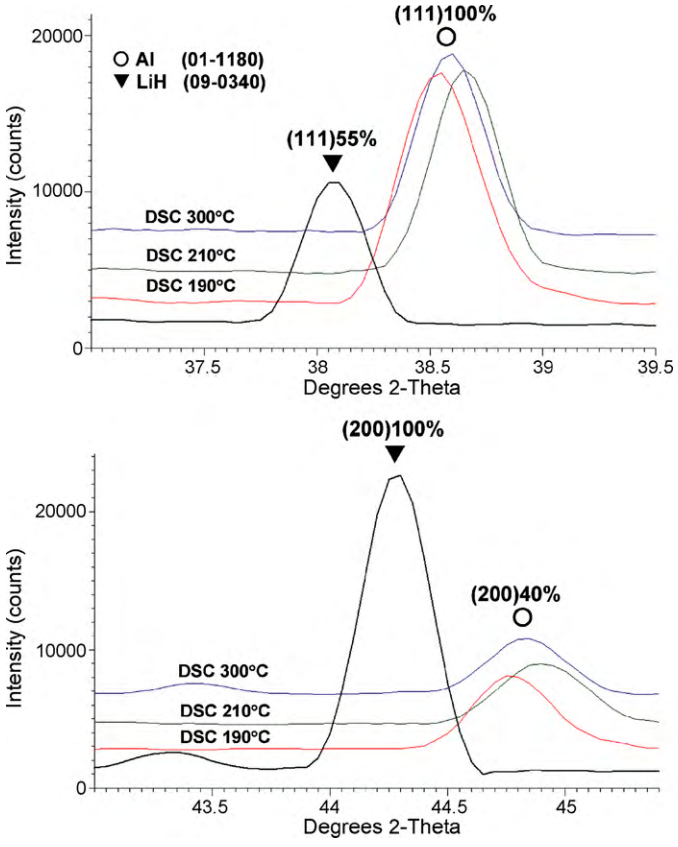

Fig. 9. Enlargement of Al peaks (1 1 1) and (2 0 0) from XRD patterns for DSC thermal sectioning test up to 190, 210 and 300 °C with overlapped XRD (1 1 1) and (2 0 0) peaks of as received LiH.

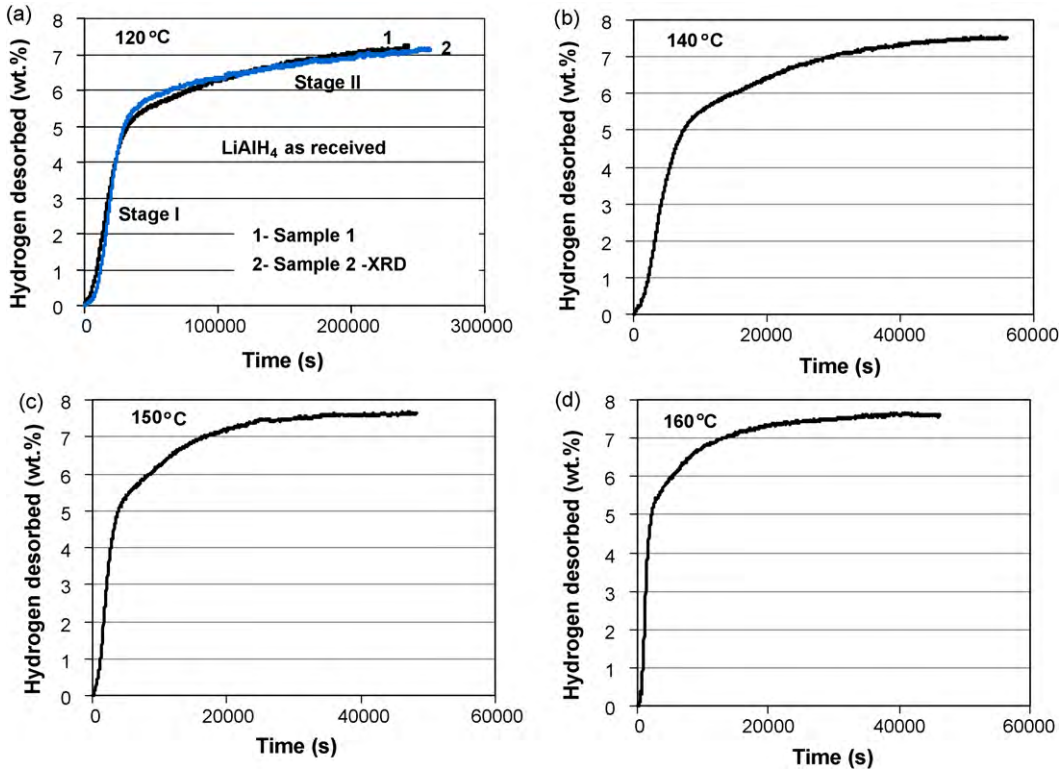

Fig. 10. Volumetric desorption curves for as received $LiAlH_4$ under 0.1MPa H_2 pressure (atmospheric) at (a) 120 °C up to 259,000 s (desorbed 7.1 wt.%H_2), (b) 140 °C up to 53,000 s (desorbed 7.5 wt.%H_2), (c) 150 °C up to 48,000 s (desorbed 7.7 wt.%H_2) and (d) 160 °C up to 46,000 s (desorbed 7.6 wt.%H_2).

of reaction (5) (Fig. 7b), shows a clear presence of the Li_3AlH_6 and Al phases and no presence of $LiAlH_4$. This means that $LiAlH_4$ starts decomposing very fast into Li_3AlH_6 immediately after melting and a half way at a temperature between peaks (2) and (3), $LiAlH_4$ is already fully decomposed. This also implies that Li_3AlH_6 is already solidified before it starts decomposing. Therefore, it seems that the exothermic character of peak (3) (Figs. 5a and 7) may not only arise due to the exothermic decomposition of $LiAlH_4$ as reported in the literature [1] but also due to the exothermic solidification event of Li_3ALH_6, i.e. these two exo events possibly superimpose. The sample heated to 210 °C beyond the peak (3) of the supposed reaction (6) (Fig. 7c) shows in Fig. 8 very weak diffraction peaks of Li_3AlH_6, strong diffraction peaks of Al and quite pronounced diffraction peaks of LiOH. It is clear that in the temperature range between 190 and 210 °C, i.e. between peaks (2) and (3), the majority of Li_3AlH_6 is already decomposed. The XRD of the sample heated up to 300 °C, i.e. beyond the peak (4) of the supposed reaction (7), shows the presence of only Al, LiOH and possibly Li and no presence of Li_3AlH_6 (observed Cu peak arises from the substrate in the environmental holder). It is clear then that the endothermic peak (4) is related to the decomposition of the small amount of remaining Li_3AlH_6 rather than the bulk of this phase as it has been a commonly held belief.

However, a completion of the decomposition of the remaining Li_3AlH_6 in reaction (7) requires the formation of LiH whose peaks are evidently not present in the XRD patterns in Fig. 8 after DSC

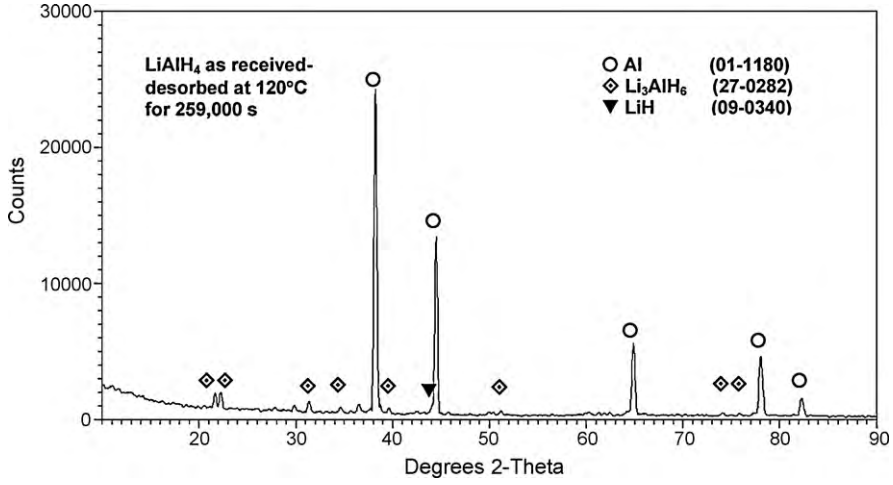

Fig. 11. XRD pattern of as received $LiAlH_4$ powder desorbed at 120 °C for 259,000 s (desorption curve in Fig. 10a). JCPDS file numbers for phase identification are given in parenthesis.

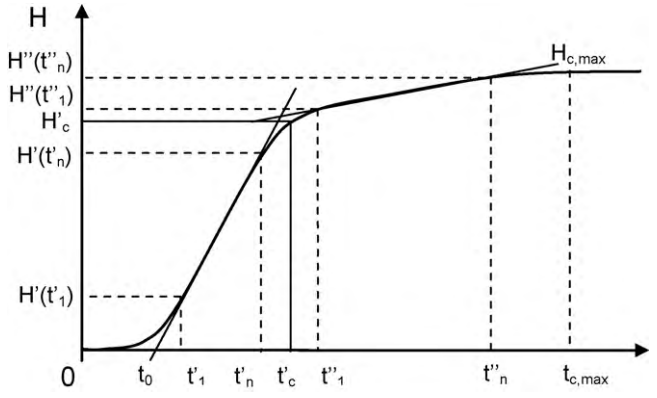

Fig. 12. A schema showing the times of the start and end of the decomposition reaction as well as maximum capacities in Stage I and II. H – instantaneous desorption capacity, $H_{c,max}$ – total maximum hydrogen desorption capacity.

test up to 210 and 300 °C. It has been argued in the literature (e.g. [4,9]) that the Bragg peaks of Al and LiH superimpose to such an extent that it is impossible to discern between them. In order to verify this notion we enlarged (1 1 1) and (2 0 0) Al peaks from the XRD patterns taken from the powders after DSC up to 190, 210 and 300 °C and superimposed on them the peaks of as received LiH as shown in Fig. 9. It is clear that the Al and LiH peak positions are split to the extent that their differentiation should not create any serious problem. As such Fig. 9 confirms that there is, indeed, no LiH present after decomposition of Li_3AlH_6 in a DSC test (Fig. 8). Despite the precautions taken some air might have leaked into an XRD environmental holder hydrolyzing LiH in the powder and converting it into LiOH whose peaks are clearly seen in Fig. 8 after DSC tests at 210 and 300 °C. If a few powder particles were inadvertently embedded in the internal rubber O-ring during loading the powder into the XRD holder in a glove box the lower and upper part of the holder might not be tightly sealed allowing some minutiae air leakage into the sample chamber. From our work on the properties of LiH which will be published separately we have found that LiH is extremely sensitive to even minutiae quantities of moisture in atmosphere immediately converting partially into LiOH.

3.3. Volumetric desorption behavior, apparent activation energy for hydrogen desorption and corresponding microstructural evolution

Fig. 10 shows the volumetric desorption curves (Sieverts) of as received $LiAlH_4$ obtained at various, relatively low temperatures, which are lower or only slightly higher than the temperature of peak (1) in Figs. 5 and 7. All desorption temperatures are decidedly below the melting peak (2) of $LiAlH_4$. All desorption curves clearly exhibit a two-stage desorption process as designated by Stage I and II in Fig. 10a. The most striking discovery observed in Fig. 10a is that as received $LiAlH_4$, fully in a solid state, is able to desorb at 120 °C under pressure of 0.1 MPa H_2 as much as 7.1 wt.%H_2 after ~259,000 s (~72 h), i.e. ~93% of the purity-corrected H_2 content from reactions (6) and (7). This is just a matter of appropriately long desorption time. So far, such a result has never been reported. In order to confirm this behavior we conducted a second desorption test which resulted in a nearly the same desorption curve 2 as compared to the curve 1 of the first test. The powder from sample 2 after desorption for ~72 h was tested by XRD as indicated in the legend in Fig. 10a. Since reaction (6) alone (now in solid state) would provide only 5.3 wt.%H_2, therefore, the amount of ~7.1 wt.%H_2 desorbed at 120 °C clearly shows that desorption process must have passed through reaction (6) fully and reaction (7) partially, i.e. Stage I and

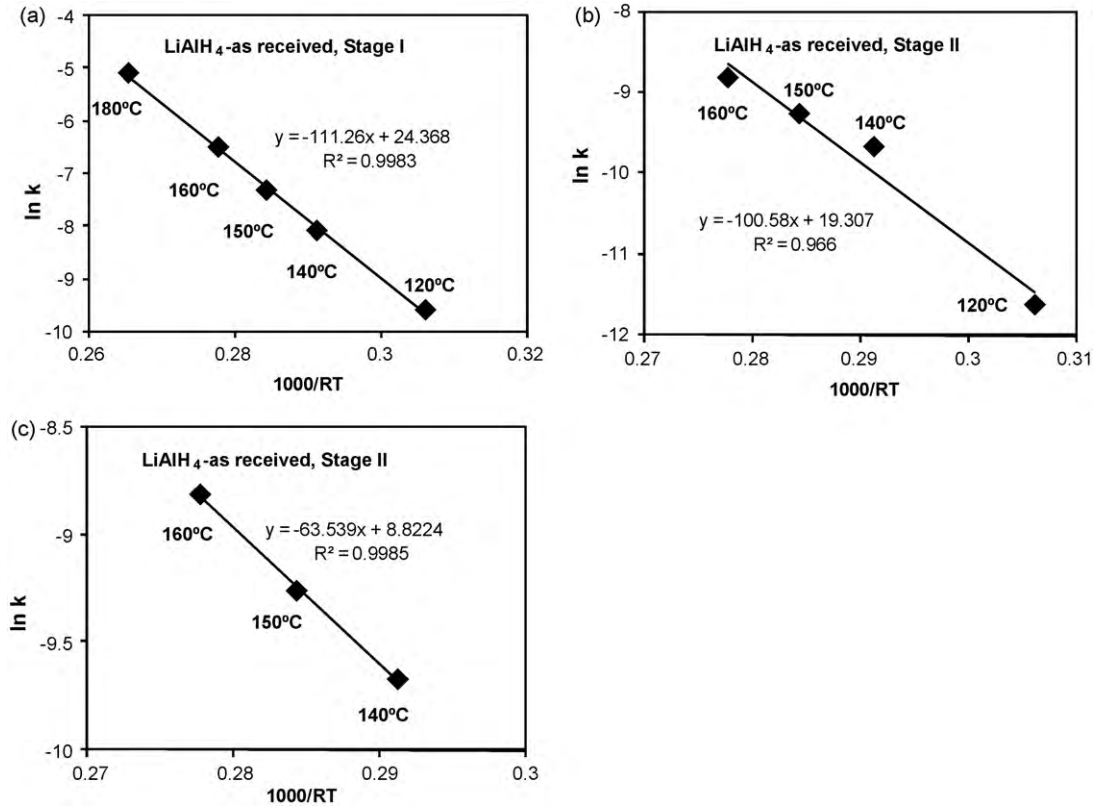

Fig. 13. The Arrhenius plots of rate constant k with temperature for calculating the activation energy of hydrogen desorption for as received $LiAlH_4$. (a) Stage I and (b and c) Stage II at a desorption curve.

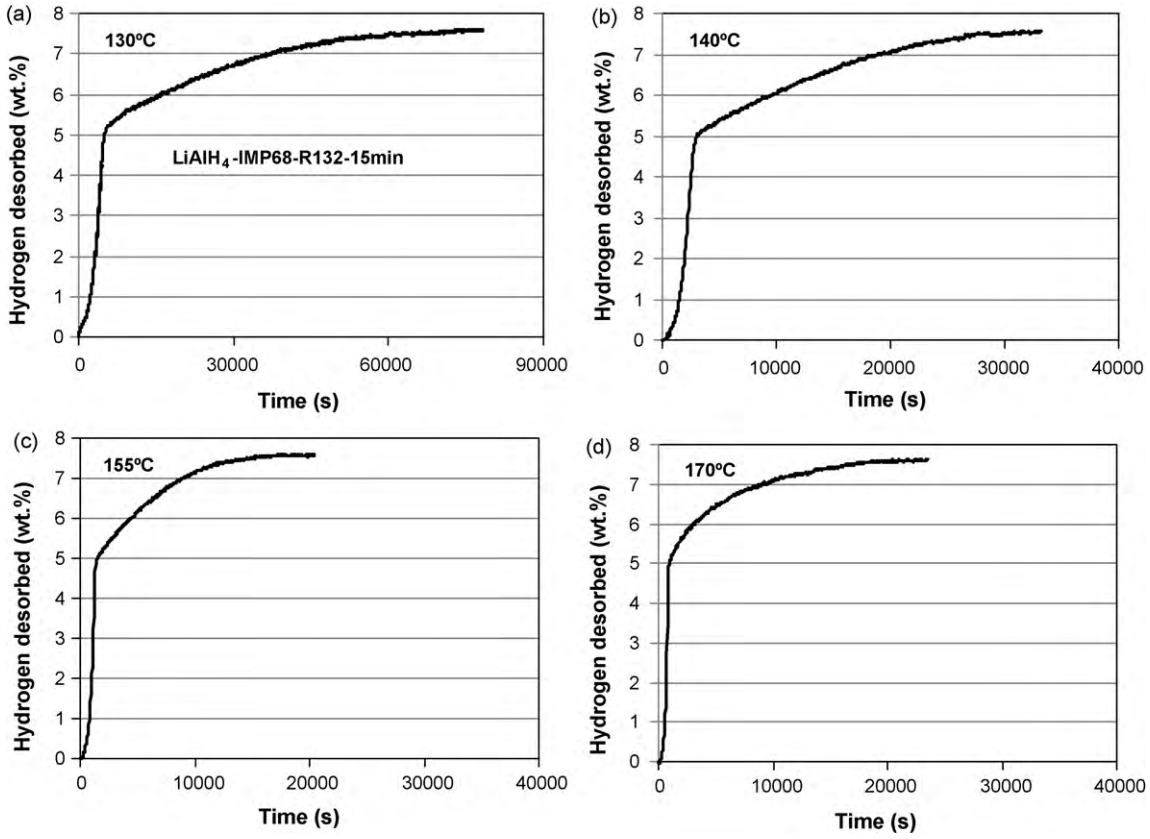

Fig. 14. Volumetric desorption curves under 0.1 MPa H_2 pressure (atmospheric) at (a) 130 °C up to 78,000 s (desorbed 7.4 wt.%H_2), (b) 140 °C up to 32,000 s (desorbed 7.5 wt.%H_2), (c) 155 °C up to 17,000 s (desorbed 7.6 wt.%H_2) and (d) 170 °C up to 23,000 s (desorbed 7.6 wt.%H_2) for $LiAlH_4$ ball milled for 15 min under high energy impact IMP68 mode with R132.

II, without any melting of the sample as the desorption temperature is much below the melting point observed in Figs. 5 and 7. Increasing desorption temperatures to 140, 150 and 160 °C slightly increases the quantity of desorbed hydrogen to 7.5, 7.7 and 7.6 wt.% and substantially reduces the desorption time to ~53,000, 48,000 and 46,000 s, respectively. The quantities of desorbed H_2 (~100% of the purity-corrected H_2 content) clearly indicate that at temperatures higher than 120 °C the desorption process must also have passed through reaction (6) and nearly fully completed reaction (7). These observations clearly show that a $LiAlH_4$ powder can desorb a nearly full purity-corrected quantity of hydrogen under 0.1 MPa pressure of H_2 due to the decomposition of both $LiAlH_4$ and Li_3AlH_6 and remain in *a solid state* throughout the entire decomposition process. An XRD pattern in Fig. 11 obtained from a powder decomposed at 120 °C confirms this notion. Very strong Al peaks and weak peaks of Li_3AlH_6 are observed which indicate that the powder is near the completion of reaction (7). A small shoulder is observed near the foot of the (2 0 0) Al peak which corresponds to the exact position of (2 0 0) 100% intensity peak of LiH. In addition, visual observations of the granular nature of the decomposed powder clearly confirm that no melting occurred during desorption at the 120–160 °C range.

In order to get rid of the initial slack (incubation period) in the desorption curves, usually appearing at low desorption temperatures (e.g. Fig. 10a), the zero time for calculations with Eq. (3) was taken at the intersection of the tangent line to the linear portion of

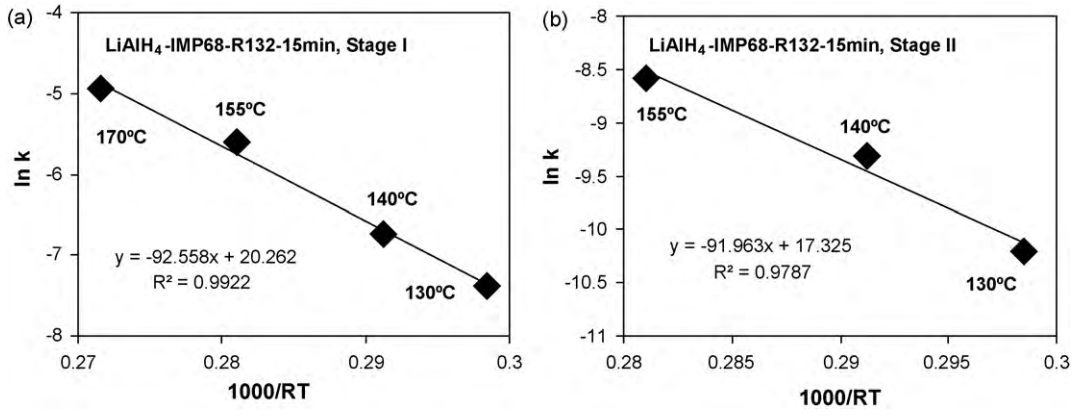

Fig. 15. The Arrhenius plots of rate constant *k* with temperature for estimation of the activation energy of hydrogen desorption for ball milled $LiAlH_4$. (a) Stage I and (b) Stage II at a desorption curve.

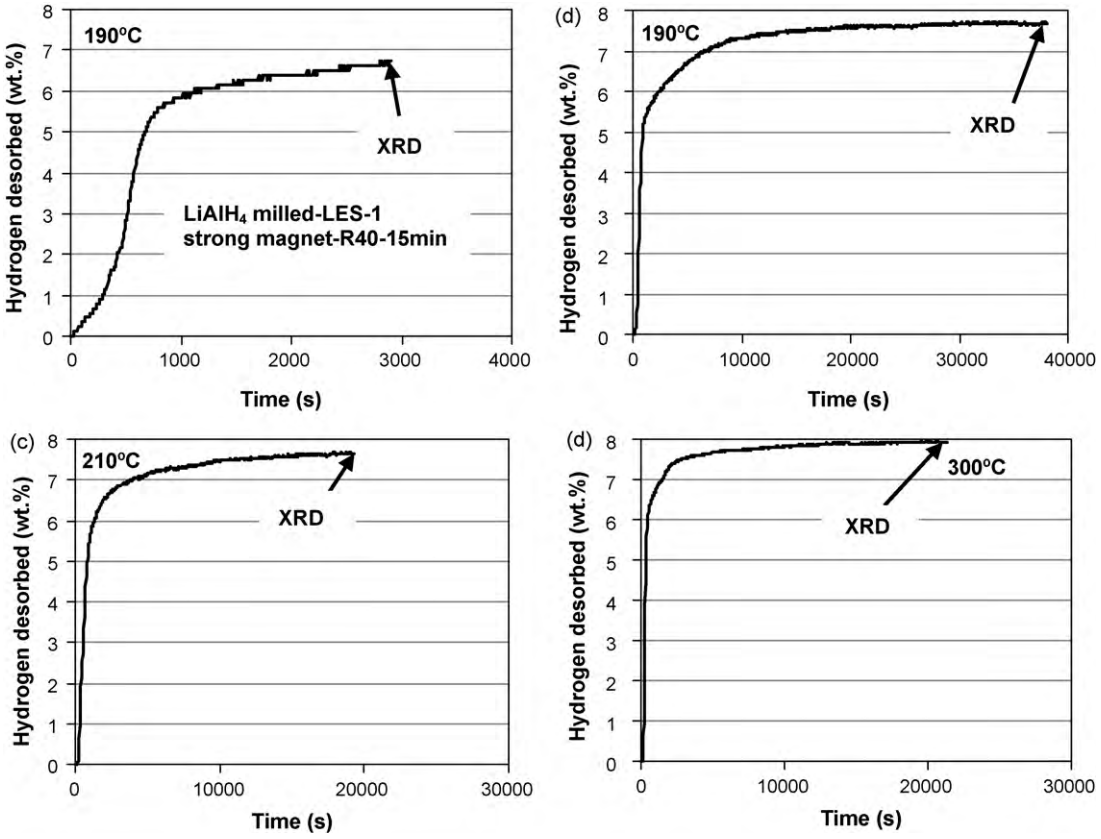

Fig. 16. Volumetric desorption curves under 0.1 MPa H_2 pressure (atmospheric) at (a) 190 °C up to 2900 s (desorbed 6.7 wt.%H_2), (b) 190 °C up to 38,000 s (desorbed 7.7 wt.%H_2), (c) 210 °C up to 19,300 s (desorbed 7.6 wt.%H_2) and (d) 300 °C up to 21,400 s (desorbed 7.9 wt.%H_2) for $LiAlH_4$ ball milled for 15 min under low energy shearing (LES) with one strong magnet and R40.

the desorption curve and the time axis as shown schematically in Fig. 12. Subsequently, for Stage I decomposition, start of the reaction is counted from time t_0 such that $t_1' - t_0$, $t_n' - t_0$, etc. and a maximum capacity for this stage is taken as H_c'. For Stage II decomposition, start of the reaction is counted from time t_c' such that $t_1'' - t_c'$, $t_n'' - t_c'$, etc. with a maximum capacity for this stage calculated as $(H_{c,max} - H_c')$ where $H_{c,max}$ is a total hydrogen desorption capacity. The free reaction exponent η for each temperature [1,14] and the corresponding rate constant k in Eq. (3) are calculated from a linear interpolation of the typical plots $\ln[-\ln(1-\alpha)]$ vs. $\ln t$ [1]. The instantaneous value of α at any time t between t_1' and t_n' is calculated as $\alpha = H(t)/H_c'$ for Stage I and between t_1'' and t_n'' as $\alpha = H(t)/(H_{c,max} - H_c')$ for Stage II.

Fig. 13 shows the Arrhenius plots for the estimate of the apparent activation energy for as received $LiAlH_4$ in Stage I and II which also shows excellent coefficients of fit to Eq. (2) giving a testimony to the accuracy of the method. Fig. 13a shows that for Stage I (reaction (6) in a solid state) the apparent activation energy is ~111 kJ/mol. Fig. 13b and c shows that for Stage II (reaction (7)) quite dissimilar apparent activation energies are obtained when the apparent activation energy is calculated either from 4 desorption curves at 120, 140, 150 and 160 °C or from 3 desorption curves at 140, 150 and 160 °C. From 4 desorption curves a value of ~100 kJ/mol is obtained vis-à-vis ~63.5 kJ/mol for 3 curves. Such a problem has been encountered from time to time in our research on solid state hydrogen storage [1] which shows that one must exercise an utmost care in the estimate of apparent activation energy since the slope of the Arrhenius plot is very sensitive to very small changes in the position of experimental data points (i.e. temperatures taken for the estimate). Since in both cases the coefficient of fit R^2 in the Arrhenius plot is very good, it is hard to make a clear judgment which value is more correct just based on the value of R^2. A common sense must prevail.

The obtained values of apparent activation energy can be compared with those reported in the literature. For Stage I (reaction (6)) the following values were reported: ~122 kJ/mol (Kissinger method) [1], ~99.6 kJ/mol (isothermal) [4], ~82 kJ/mol (a single desorption curve fitting) [8], ~115 kJ/mol (Kissinger method) [9], ~81 kJ/mol (Kissinger method) [20], and ~102 kJ/mol ($LiAlD_4$; synchrotron X-ray diffraction method) [21]. By comparison, the value of apparent activation energy obtained in the present work for Stage I is slightly higher than that reported in [21] and slightly lower than that reported in [1,9]. However, we do not support a conclusion derived by Ares et al. [9] who claimed on the basis of apparent activation energy values measured at low and high heating rates in DSC that the release of hydrogen after melting is more favorable than the release of hydrogen without melting. In our case hydrogen was released in Stage I (reaction (6)) without melting with the apparent activation energy of ~111 kJ/mol which compares very well with the apparent activation energy of ~115 kJ/mol reported by Ares et al. [9] for the decomposition after melting. It seems clear to us that there is no such a great difference between the apparent activation energy of decomposition of $LiAlH_4$ into Li_3AlH_6 in a solid and molten state.

For Stage II (reaction (7)) the following values of apparent activation energy were reported: ~153 kJ/mol (Kissinger method) [1], ~196 kJ/mol (isothermal) and ~100 kJ/mol (Kissinger method) [4], ~90 kJ/mol (a single desorption curve fitting) [8], ~86 kJ/mol (Kissinger method) [9], and ~108 kJ/mol (Kissinger method) [20]. Our present value of ~100 kJ/mol compares favorably with nearly all the literature reported values except ~153 kJ/mol in [1] and ~196 kJ/mol in [4] which seem to be

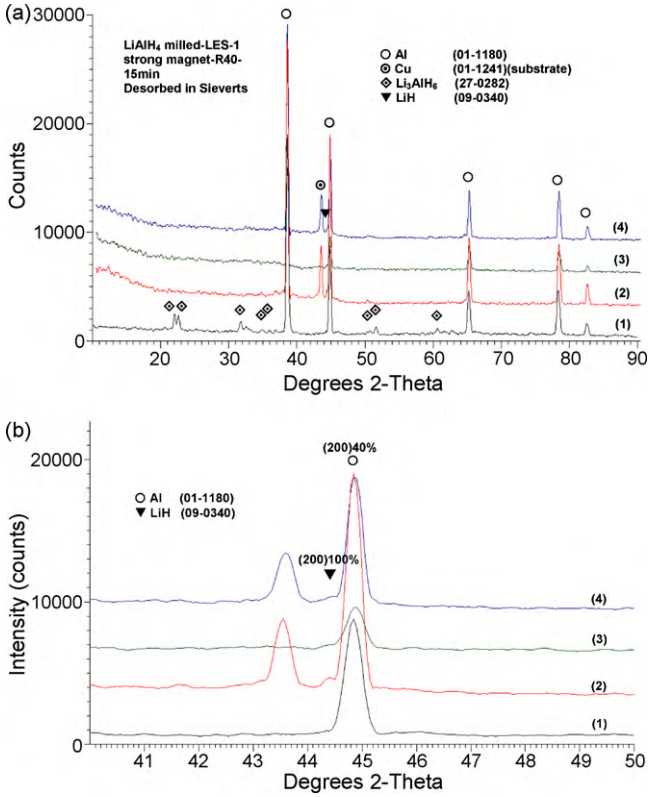

Fig. 17. (a) XRD patterns of powders desorbed in a Sieverts-type apparatus for $LiAlH_4$ ball milled for 15 min under low energy shearing (LES) with one strong magnet and R40 from Fig. 16. Pattern (1): 190 °C (Fig. 16a); pattern (2): 190 °C (Fig. 16b); pattern (3): 210 °C (Fig. 16c); pattern (4): 300 °C (Fig. 16d). (b) Enlargement of the (2 0 0) Al peak to show small shoulders at the position of the (2 0 0) 100% intensity peak of LiH. JCPDS file numbers for phase identification are given in parenthesis.

much higher. Also, from this comparison it seems that the value of ~63.5 kJ/mol obtained here from desorption curves at 3 different temperatures in Fig. 13c is rather unreasonably low.

Fig. 14 shows the volumetric desorption curves (Sieverts apparatus) for $LiAlH_4$ ball milled under high energy impact IMP68 mode obtained at relatively low temperatures, which are lower than the melting peak (2) of $LiAlH_4$ in Figs. 5 and 7. By comparison with Fig. 10 at similar temperatures it seems that the desorbed amount of ~7.5 wt.%H_2 is achieved in a shorter time than the time needed to desorb the same quantity of H_2 from as received $LiAlH_4$ (Fig. 10). The Arrhenius plots for the estimate of apparent activation energy of ball milled $LiAlH_4$ are shown in Fig. 15. Fig. 15a shows that for Stage I (reaction (6) in a solid state) the apparent activation energy is ~92.6 kJ/mol and Fig. 15b shows that that for Stage II (reaction (7)) the apparent activation energy is ~92 kJ/mol. Both values are quite similar but slightly lower than the corresponding values for as received $LiAlH_4$ which is in accord with slightly faster desorption rates observed in Fig. 14 as compared to Fig. 10.

In order to investigate desorption behavior and microstructural evolution at higher temperatures a $LiAlH_4$ powder ball milled under low energy shearing (LES) was desorbed at 190 °C up to 2900 s with 6.7 wt.%H_2 desorbed (Fig. 16a), at 190 °C up to 38,000 s with 7.7 wt.%H_2 desorbed (Fig. 16b), at 210 °C up to 19,300 s with 7.6 wt.%H_2 desorbed (Fig. 16c) and at 300 °C up to 21,400 s with 7.9 wt.%H_2 desorbed (Fig. 16d). The quantities of hydrogen desorbed at 190–300 °C clearly show that at these temperatures after the corresponding time durations used for desorption, reactions (6) and (7) were, indeed, completed. In this case, visual observations of the lumped nature of the decomposed powder indicates that some melting occurred during isothermal desorption in a Sieverts-type apparatus at temperatures of 190 °C and higher.

After desorption the powders were tested by XRD and the corresponding patterns are shown in Fig. 17a. After desorption at 190 °C for 2900 s (pattern (1)) the microstructure comprises a small amount of Li_3AlH_6 (very weak peaks) and Al. It indicates that reaction (6) is near completion. After desorption at 190 °C for 38,000 s and at 210 and 300 °C for corresponding times (patterns (2), (3) and (4)) the microstructure contains Al and possibly LiH. In order to elucidate the presence of LiH, the (2 0 0) Al peak was enlarged and is shown in Fig. 17b. A small "shoulder" is observed at the foot of the (2 0 0) Al peak which corresponds very well to the position of (2 0 0) 100% intensity peak of LiH. Therefore, it is quite likely that some amount of LiH is present in the microstructure indicating that, indeed, reaction (7) was completed. However, surprisingly the (2 0 0) 100% peak of LiH has really low intensity. It is not clear if this is related to an X-ray absorption mechanism specific to LiH or its partial amorphization although we did not observe any amorphization of pristine LiH under high energy ball milling (a paper in preparation for publication).

It must also be pointed out that the microstructural investigations by XRD presented in Fig. 11 do not support a notion that the thermal decomposition of $LiAlH_4$ in a solid state may follow a

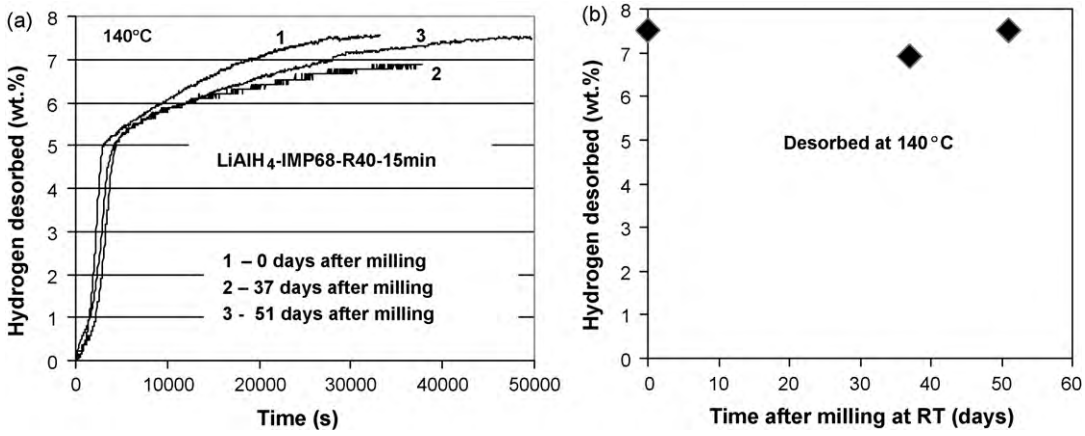

Fig. 18. (a) Desorption curves of $LiAlH_4$ ball milled for 15 min under high energy impact IMP68 mode with R40 and stored for 37 and 51 days at room temperature (RT) as compared to desorption curve of powder after milling (0 days). (b) Desorbed hydrogen capacity of long-term stored ball milled powder of $LiAlH_4$ vs. storage time at room temperature (RT) after milling.

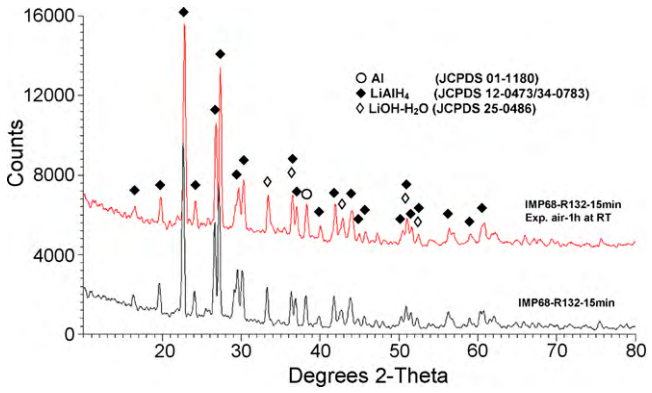

Fig. 19. XRD pattern of $LiAlH_4$ ball milled for 15 min under high energy impact IMP68 mode with R132 and XRD pattern of the same ball milled powder exposed to 47% humid air for 1 h which resulted in water absorption of 11.7%. JCPDS file numbers for phase identification are given in parenthesis.

direct decomposition path into LiH and Al as suggested by Wiench et al. [22]. Our observations show the presence of an intermediate Li_3AlH_6 phase in Fig. 11.

3.4. The effects of long-term storage on hydrogen capacity

Some researchers have reported that pristine $LiAlH_4$ is inherently thermodynamically unstable and spontaneously decomposes into Li_3AlH_6 after long-term storage at room temperature [18,23,24]. We decided to investigate a long-term stability of ball milled $LiAlH_4$ in more detail. A powder was ball milled under IMP68 mode with R40 for 15 min and about 50 mg of ball milled powder was loaded into a glass vial in a glove box purged with ultra-high purity argon. The loaded vial was stored in a glove box and samples for volumetric desorption tests in a Sieverts-type apparatus were taken after 37 and 51 days of storage. Desorption was carried out at 140 °C for such a duration of time until desorption curves achieved saturation as shown in Fig. 18a for desorption curves after 37 and 51 days compared to desorption curve tested shortly after milling (0 days). Fig. 18b shows a plot of desorbed capacity of H_2 as a function of storage time at room temperature. It is quite clear that up to 51 days of storage there is no measurable loss of H_2 capacity due to room temperature storage which is close to 7.5 wt.%, i.e. the same as after milling. Only rate of desorption after 51 days of storage seems to be slightly slower than that after milling (Fig. 18a). Slightly lower capacity of 6.9 wt.%H_2 in Fig. 18b was obtained after 37 days simply because the test was stopped too early before the desorption curve could reach saturation as can be clearly seen in Fig. 18a. Therefore, one can conclude that the thermodynamic stability of ball milled $LiAlH_4$ with much reduced particle size which is composed of nanograins is quite good at least up to approximately 2 months of storage at room temperature in argon atmosphere. The observed behavior is definitely in contrast to the storage of catalyzed $LiAlH_4$ which looses a substantial quantity of H_2 within a comparable storage time at room temperature (a paper in preparation for publication).

3.5. The effects of moisture absorption on microstructure and hydrogen capacity

$LiAlH_4$ is perceived as a very reactive hydride [1] particularly very sensitive to contact with water or moisture. In order to have some assessment how exposure to moisture can affect hydrogen storage properties of $LiAlH_4$ the powder was ball milled for 15 min (to sensitize it even more by refining the particle size) under high energy impact IMP68 mode with R132. Subsequently, some amount of ball milled powder was weighed in a glove box and then exposed to air in a fume hood with relative humidity of 47% for 1 h. After completion of the exposure the powder was weighed again and the relative mass increase due to water absorption came up to 11.7%. Fig. 19 shows an XRD pattern of sample which absorbed 11.7% water compared to an XRD of sample ball milled for 15 min under high energy impact IMP68 mode with R132. As can be seen the XRD pattern after water absorption is not changed in any measurable way as compared to its ball milled counterpart. Fig. 20 compares hydrogen desorption curve for ball milled sample of virgin $LiAlH_4$ with the one for a sample which absorbed 11.7% water. A virgin ball milled sample and a sample which absorbed 11.7% water desorbs 5 wt.%H_2 within ~11,000 and 11,500 s, respectively. It seems that the water absorption up to 11.7% does not change in any drastic way the desorption rate of ball milled $LiAlH_4$ in Stage I, i.e. reaction (6).

3.6. Flammability assessment

When the milling cylinder with the ball milled $LiAlH_4$ is opened in a glove box under Ar atmosphere, there is no evidence of self-ignition. Furthermore, flammability studies also show that the ball milled $LiAlH_4$ does not ignite spontaneously after opening the milling cylinder in air. However, within 15 min from the opening of the milling cylinder the powder can be ignited by scraping the cylinder walls with a metal tool and then the powder burns with an open flame. This behavior indicates that even ball milled $LiAlH_4$

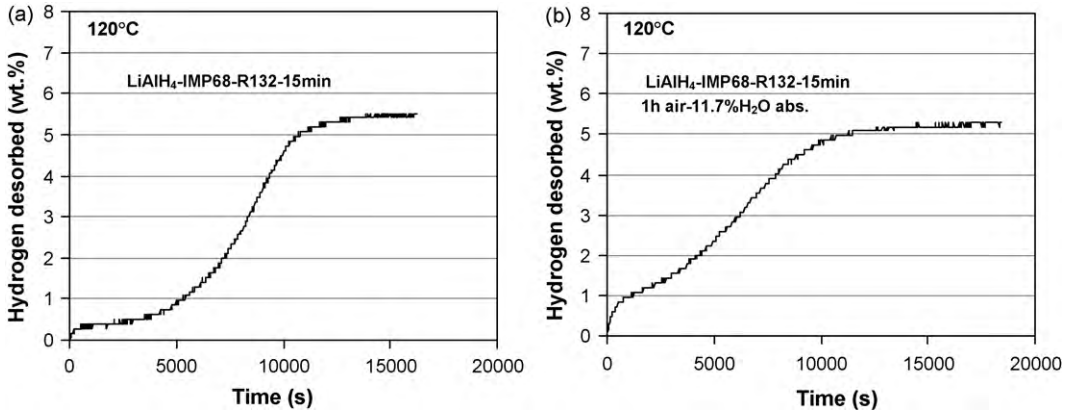

Fig. 20. (a) Desorption curve at 120 °C under 0.1 MPa H_2 pressure for $LiAlH_4$ ball milled for 15 min under high energy impact IMP68 mode. (b) Desorption curve at 120 °C under 0.1 MPa H_2 pressure for $LiAlH_4$ ball milled for 15 min under high energy impact IMP68 mode and exposed to 47% humid air for 1 h which resulted in water absorption of 11.7%.

with greatly reduced particle size is a relatively benign hydride not really prone to self-ignition on contact with air always containing some amount of moisture.

4. Conclusions

The more important conclusions are as follows:

(1) From the comparison of microstructural investigations of the present $LiAlH_4$ with those reported by Ares et al. [9] it is clear that the morphology, microstructure and chemistry of $LiAlH_4$ can be very dissimilar depending on the supplier from which $LiAlH_4$ powder was purchased. These differences may influence thermal desorption behavior.
(2) The average ECD particle size with standard deviation of $LiAlH_4$ ball milled for 2 h under high energy mode IMP68 mode with R132 in this work is $2.8 \pm 2.3\,\mu m$ which is much smaller than the average particle size reported by Ares et al. [9] who investigated Sigma–Aldrich $LiAlH_4$.
(3) We do not observe a partial decomposition of $LiAlH_4$ during milling up to 5 h under high energy impact mode.
(4) The melting of $LiAlH_4$ in a DSC test is a very volatile event. Immediately after the beginning of melting the liquid $LiAlH_4$ starts foaming and flowing out of the alumina crucible raising the alumina lid. After completion of desorption and solidification the powder resembles a lava rock.
(5) Thermal sectioning in DSC combined with a phase analysis using XRD shows that $LiAlH_4$ starts decomposing into Li_3AlH_6 immediately after transforming to a melt and half way at a temperature between the temperature peak of the reaction $LiAlH_4(s) \rightarrow LiAlH_4(l)$ and $LiAlH_4(s) \rightarrow (1/3)Li_3AlH_6(s) + (2/3)Al(s) + H_2$, $LiAlH_4$ is already fully decomposed. This also implies that Li_3AlH_6 formed is already solidified when it starts decomposing.
(6) All volumetric desorption curves clearly exhibit a two-stage desorption process, Stage I and II. The most striking discovery is that as received $LiAlH_4$ is able, in a fully solid state, to desorb at 120 °C under pressure of 0.1 MPa H_2 (atmospheric) as much as 7.1 wt.%H_2 within ~259,000 s (~72 h), i.e. 93% of the purity-corrected H_2 content from reaction in Stage I ($LiAlH_4(s) \rightarrow (1/3)Li_3AlH_6(s) + (2/3)Al(s) + H_2$) and II ($(1/3)Li_3AlH_6 \rightarrow LiH + (1/3)Al + 0.5H_2$). The apparent activation energy for Stage I and II for unmilled $LiAlH_4$ is ~111 and ~100 kJ/mol, respectively. For ball milled $LiAlH_4$ the apparent activation energy for Stage I and II is ~92.5 and ~92 kJ/mol, respectively.
(7) The microstructural investigations presented in this work do not support a notion that thermal decomposition of $LiAlH_4$ in a solid state may follow a direct decomposition path into LiH and Al as suggested by Wiench et al. [22].
(8) It seems that the ball milled $LiAlH_4$ is reasonably immune to the exposure to most air. The water absorption up to 11.7% due to exposure to air for 1 h does not change in any drastic way the desorption rate of ball milled $LiAlH_4$ in Stage I, i.e. reaction $LiAlH_4(s) \rightarrow (1/3)Li_3AlH_6(s) + (2/3)Al(s) + H_2$.
(9) The ball milled $LiAlH_4$ powder does not ignite spontaneously by simply opening a milling cylinder in air. However, within approximately 15 min from the opening of the milling cylinder the ball milled $LiAlH_4$ powder can be ignited by scraping the cylinder walls with a metal tool and then the powder burns with an open flame.

Acknowledgments

This research was supported by the NSERC Hydrogen Canada (H2CAN) Strategic Research Network and NSERC Discovery grants which are gratefully acknowledged. The authors are grateful to Prof. Linda Nazar from the Department of Chemistry, University of Waterloo, for the usage of XRD equipment. The authors thank Prof. A. Calka from the University of Wollongong for XRD calculations.

References

[1] R.A. Varin, T. Czujko, Z.S. Wronski, Nanomaterials for Solid State Hydrogen Storage, Springer Science+Business Media, New York, NY, 2009.
[2] J. Graetz, J.J. Reilly, Scr. Mater. 56 (2007) 835–839.
[3] J. Block, A.P. Gray, Inorg. Chem. 4 (1965) 304–305.
[4] M. McCarty Jr., J.N. Maycock, V.R. Pai Verneker, J. Phys. Chem. 72 (1968) 4009–4014.
[5] J.A. Dilts, E.C. Ashby, Inorg. Chem. 11 (1972) 1230–1236.
[6] V.P. Balema, V.K. Pecharsky, K.W. Dennis, J. Alloys Compd. 313 (2000) 69–74.
[7] H.W. Brinks, B.C. Hauback, P. Norby, H. Fjellvåg, J. Alloys Compd. 351 (2003) 222–227.
[8] A. Andreasen, T. Vegge, A.S. Pedersen, J. Solid State Chem. 178 (2005) 3672–3678.
[9] J.R. Ares, K.-F. Aguey-Zinsou, M. Porcu, J.M. Sykes, M. Dornheim, T. Klassen, R. Bormann, Mater. Res. Bull. 43 (2008) 1263–1275.
[10] A. Calka, A.P. Radlinski, Mater. Sci. Eng. A 134 (1991) 1350–1353.
[11] Patents: WO9,104,810, US5,383,615, CA2,066,740, EP0,494,899, AU,643,949.
[12] A. Calka, R.A. Varin, in: T.S. Srivatsan, R.A. Varin, M. Khor (Eds.), International Symposium on Processing and Fabrication of Advanced Materials IX (PFAM IX), ASM International, Materials Park, OH, 2001, pp. 263–287.
[13] H.P. Klug, L. Alexander, X-ray Diffraction Procedures for Polycrystalline and Amorphous Materials, John Wiley & Sons, New York, 1974, pp. 618–708.
[14] A. Calka, A.P. Radlinski, Mater. Sci. Eng. 97 (1988) 241–246.
[15] NIST/SEMATECH e-Handbook of Statistical Methods, http://www.itl.nist.gov/div898/handbook/eda/section3/eda366g.htm.
[16] D. Blanchard, H.W. Brinks, B.C. Hauback, P. Norby, Mater. Sci. Eng. B 108 (2004) 54–59.
[17] J.-P. Bastide, B. Bonnetot, J.-M. Lettofé, P. Claudy, Mater. Res. Bull. 20 (1985) 999–1007.
[18] S.-I. Orimo, Y. Nakamori, J.R. Eliseo, A. Züttel, C.M. Jensen, Chem. Rev. 107 (2007) 4111–4132.
[19] O.M. Løvvik, S.M. Opalka, H.W. Brinks, B.C. Hauback, Phys. Rev. B 69 (2004) 134117-1–134117-9.
[20] A. Andreasen, J. Alloys Compd. 419 (2006) 40–44.
[21] D. Blanchard, H.W. Brinks, B.C. Hauback, P. Norby, J. Muller, J. Alloys Compd. 404–406 (2005) 743–747.
[22] J.W. Wiench, V.P. Balema, V.K. Pecharsky, M. Pruski, J. Solid State Chem. 177 (2004) 648–653.
[23] D. Blanchard, A.I. Lem, S. Øvergaard, H.W. Brinks, B.C. Hauback, J. Alloys Compd. 458 (2008) 467–473.
[24] T.J. Francombe, G.-J. Kroes, Chem. Phys. Lett. 423 (2006) 102–105.